Magnetic Torque Compensating Methods for Cam Indexing Devices

Kuang-Yuh Huang, Pei-Chuan Lin, and Sheng-Fu Tsai

Department of Mechanical Engineering National Taiwan University, Taipei 10764, Taiwan, R.O.C.

In automatic production processes, cam indexing devices are frequently utilized to transport workpieces intermittently to the appointed manufacturing positions. However, because of alternating working forces and rotational inertia, indexing devices tend to generate vibration during each positioning process, which retards working speed and degrades positioning accuracy. To minimize positioning vibration, we developed a magnetic compensation concept and diverse devices based on the concept. A magnetic torque compensator basically consists of a magnetic loop with field generator and soft-magnetic elements. The soft-magnetic elements are designed to generate relative motion to each other to realize variable distribution of magnetic field and induce a compensation torque to suppress the positioning vibration. In addition to our experimental research, we investigated analytically the influential parameters of the compensating torque and their relationships by using the equivalent magnetic circuit method and the finite-element method. We found that modifications of magnetic arrangement or geometric parameters of functional elements lead to different characteristics of the magnetic torque curve. On the basis of the verified function and parameters of the magnetic torque compensator, we built some configurations to synthesize the compensating torque needed for countering vibration.

Index Terms—**Functional analysis, magnetic device, motion compensation, torque control.**

I. Introduction

A ROLLER gear cam, an indexing device as shown in Fig. 1(a) and (b), is widely utilized in many modern automatic production processes for intermittent transporting and positioning workpieces to the appointed working positions [1]. An ac-motor driven successive motion on the input shaft generates rotation of cam shaft; and through interactive mechanism the roller turret realizes sequential "stop-rotate-stop" stepping motions on the output shaft [2]. This intermittent reduction mechanism realizes large torque with low speed on the output shaft. Normally, the output shaft is coupled with a large heavy rotational worktable, whose inertia inversely affects the dynamics of the whole system. A reverse torque reacts on the input shaft when the output shaft starts to rotate, and a forward torque forces the input shaft to rotate forth when the output shaft halts. As shown in Fig. 1(c), each torque variation on the input shaft induces rotational vibration, which significantly influences the stability and positioning speed of the output shaft. A simple approach for countering the torque variation is the realization of a corresponding compensating torque. Sarring [3] developed a torque compensation method for cam systems. Benedict *et al.* [4] applied a sub-unit cam to balance torque in machines. Nishioka *et al.* [5]–[7] invented an attached cam compensator against the torque vibration on input shaft of roller gear cam indexing device. Tasy *et al.* [8] also realized torque-balancing cams for globoidal cam indexing mechanisms. All the above-mentioned torque compensating concepts applied mainly mechanical principles, which, nevertheless, have some inherent drawbacks such as wear, stick-slip effect, and high manufacturing cost. Other than those mechanical concepts, there are some alternatives [9]–[18] such as torque compensating servomotor control and switchable gear coupling on the output shaft.

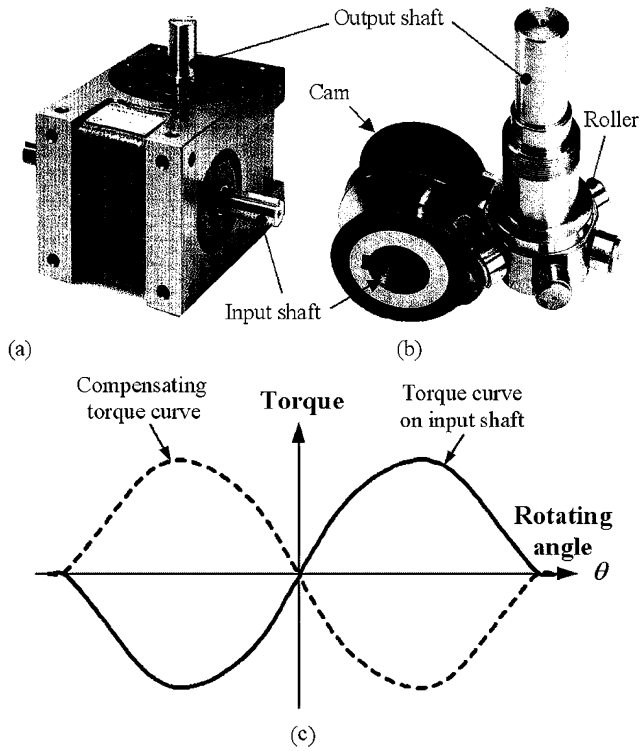

Fig. 1. Roller gear cam indexing device and torque variation on input shaft. (a) Roller gear cam indexing device. (b) Roller gear and cam.

To avoid the drawbacks induced by physical contact, we develop a novel magnetic torque compensating concept, whose basic configuration is presented in Fig. 2(a). A magnetic loop,

Digital Object Identifier 10.1109/TMAG.2006.888193

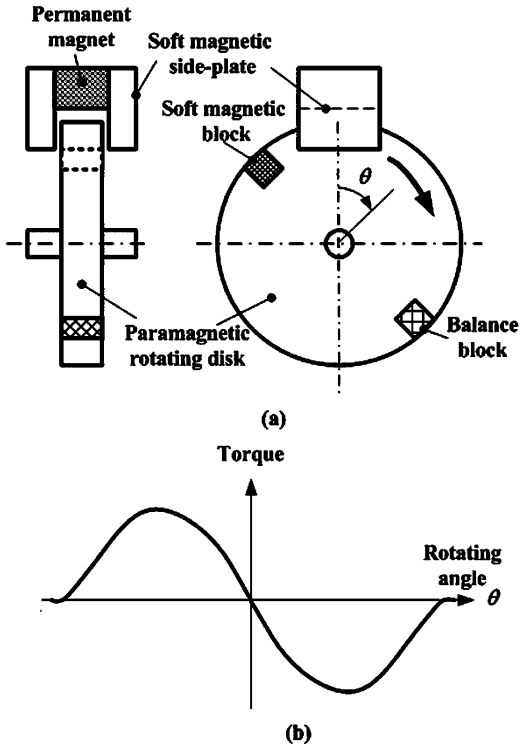

Fig. 2. Conceptual configuration and function of a magnetic torque compensator. (a) Basic conceptual configuration. (b) Magnetic compensating torque curve.

composed of a permanent magnet and two soft-magnetic side-plates, is set up as the stator, and a soft-magnetic element and a balance block are mounted on a paramagnetic rotating disk. The movement of the soft-magnetic element in the magnetic loop transforms magnetic energy into mechanical energy. When the soft-magnetic element approaches the magnetic loop, the tangential magnetic attracting force on the soft-magnetic element generates a forward torque on the rotating disk; when it leaves the magnetic loop, a reverse torque reacts on the rotating disk instead. Fig. 2(b) shows the relationship between the magnetic torque and the rotating angle of the rotating disk. The magnetic torque compensating concept, in comparison with mechanical concepts, possesses some advantages such as: 1) noncontact torque compensation; 2) no friction and wear; 3) no lubricant needed; and 4) no precise surface manufacturing for acting elements needed. Several experiments and theoretical analyses are carried out to comprehend the relationship between the magnetic torque and the design parameters of the magnetic system. Additionally, we develop several methods with modular elements to synthesize the designed compensating torque curve.

II. Functional Analysis

A. Working Principle and Influential Parameters

According to our developed basic configuration, the reaction torque is induced by the magnetic force, which is affected mainly by the magnetic flux between acting elements. Furthermore, the acting radius of the rotating disk is associated with the transformation of the magnetic force into the torque. Besides the moving distance (operational parameter), main design parameters include form, geometric parameters, and magnetic arrangement. Through systematic design approach, diverse torque compensating devices can be evolved by varying magnetic arrangement and design parameters.

Fig. 3(a) shows the relationship between the magnetic force F and the air gap $D_{\rm gap}$. A reduction of the air gap causes increase of the magnetic flux and the corresponding magnetic force F. The hystersis effect of magnetic material induces an unsymmetrical curve, while inhomogeneity of magnetic materials and slight misalignment cause a zero-point offset. All curves have almost the same peak positions at ± 10 mm, which slightly go beyond the both edges of the magnetic yoke. However, these two edges still have decisive influences on the peak positions. Fig. 3(b) shows that the shifting of the peaks is dependent on the distance of both edges $L_{\rm e}$, which is defined as a geometric parameter of the cross section of the magnetic yoke. An increase of cross section of the magnetic yoke leads to further decrease of magnetic induction, which yields a drop of the peak values and forms a flat zone in the midst of the torque curve. Fig. 3(c) shows the effect of the inclination angle $\theta_{\rm ia}$ on the magnetic force. An inclined edge allows magnetic flux to flow easily into the approaching magnetic element. A smaller inclination angle of $\theta_{\rm ia} = 5^\circ$ realizes a wider and lower plateau than that of a larger inclination $\theta_{\rm ia} = 10^\circ$, while the inclination angle has less influence on the peak position. Furthermore, the leading angle $\theta_{\rm sa}$ also governs the magnetic force, as shown in Fig. 3(d). Due to the leading angle $\theta_{\rm sa}$, the cross section of the magnetic yoke varies in proportion to the moving distance D. Therefore, on the leading edge, a gradually distributive magnetic flux broadens the active range of the magnetic force.

Besides, the arrangement of permanent magnet is closely associated with the magnetic force, as shown in Fig. 4. The magnetic flux is introduced to any designated working zone by using soft-magnetic element. In the standard arrangement (the first type), a NdFeB magnet is symmetrically installed in the middle of the magnetic yoke. And the second arrangement is reinforced by two additional magnets. However, the increase of magnets does not create obvious enhancement of magnetic force due to the presence of leakage paths on the sides of the yoke. The third arrangement puts two magnets capped with small pole pieces for protection and field guiding closely to the working air gap. Having less flux leakage, the third arrangement generates the maximum magnetic force and gives a sharp peak on the curve, which is threefold as large as those realized by the other two arrangements.

B. Theoretical Model of Magnetic Torque Compensator

In the basic configuration of the magnetic torque compensator, the magnetic loop with the working air gap is built up to accumulate the magnetic energy to transform into mechanical work for the approaching magnetic part. Fig. 5 shows the entire magnetic circuit and its equivalent circuit. The total magnetic flux Φ from the permanent magnet is divided into two fluxes: Φ_{a1} and Φ_{a2}, where Φ_{a1} passes through the air gap, and Φ_{a2} flows through the moving part

$$\Phi = \Phi_{a1} + \Phi_{a2}. \tag{1}$$

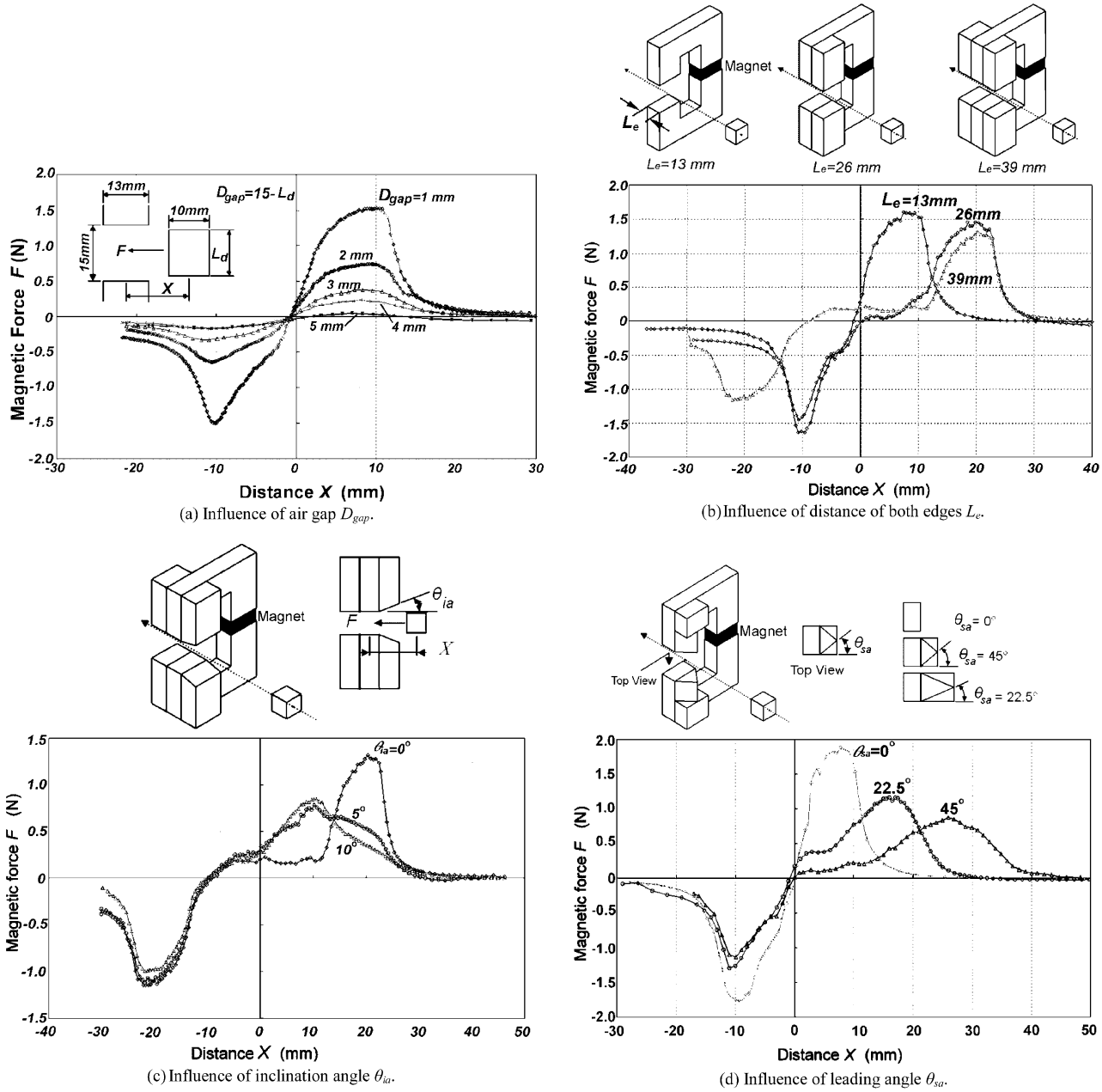

(a) Influence of air gap D_{gap}.

(b) Influence of distance of both edges L_e.

(c) Influence of inclination angle θ_{ia}.

(d) Influence of leading angle θ_{sa}.

Fig. 3. Influential parameters of magnetic force F. (a) Influence of air gap $D_{\rm gap}$. (b) Influence of distance of both edges L_e. (c) Influence of inclination angle θ_{ia}. (d) Influence of leading angle θ_{sa}.

By applying the line integral theorem, the magnetomotive force MMF from the permanent magnet can be written as follows:

$$\begin{aligned}\text{MMF} &= -H_m L_m \\ &= H_s L_s + H_{a1} L_{a1} \\ &= H_s L_s + 2H_{a2} L_{a2} + H_{d2} L_{d2}. \end{aligned} \tag{2}$$

The balanced situation of magnetic circuit varies with the distance X between the moving magnetic part and the fixed magnetic loop. Both air paths L_{a2} between the moving part and the magnetic circuit are dependent on the moving distance X. Those reluctances in the equivalent electrical circuit are described as

$$\begin{aligned}&\text{Soft-magnetic path: } R_s = L_s/\mu_0\mu_s A_s \\ &\text{Air gap a1: } R_{a1} = L_{a1}/\mu_0 A_{a1} \\ &\text{Air paths a2: } R_{a2} = L_{a2}/\mu_0 A_{a2}\sin\theta; \\ &\qquad \text{where } \theta = \arctan(D_{\rm gap}/X) \\ &\text{Moving magnetic part: } R_{d2} = L_{d2}/\mu_0\mu_{d2}A_{d2} \end{aligned} \tag{3}$$

where $A_{a2}\cdot\sin\theta$ is the average projected cross-sectional area of both magnetic poles along the flux direction, and θ is the angle between the magnetic flux and the force acting direction. From

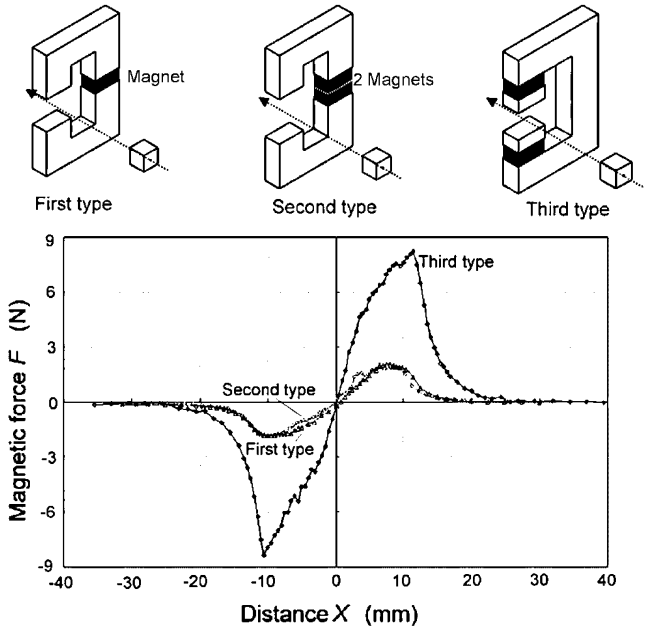

Fig. 4. Influences of magnetic arrangements on magnetic force F.

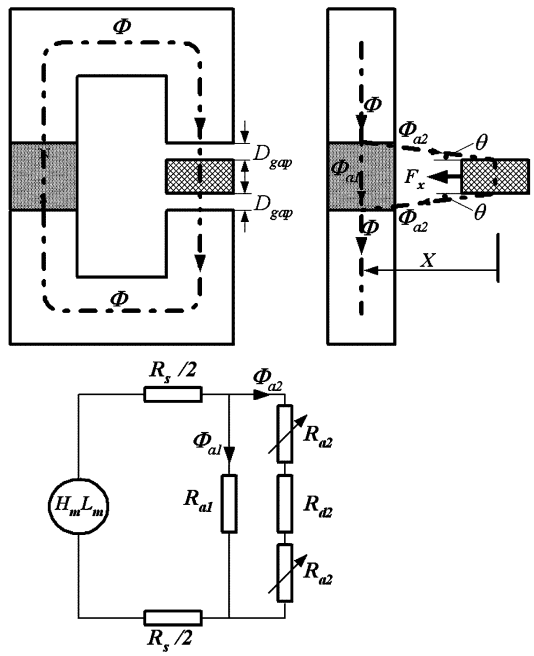

Fig. 5. Magnetic circuit and equivalent circuit.

the parameters of the permanent magnet and these reluctances, the fluxes Φ, Φ_{a1}, and Φ_{a2} can be derived

$$\Phi = \frac{H_m L_m}{\left(R_s + \frac{R_{a1}(2R_{a2}+R_{d2})}{R_{a1}+2R_{a2}+R_{d2}}\right)} \tag{4}$$

$$\Phi_{a1} = \frac{H_m L_m - \Phi R_s}{R_{a1}} \tag{5}$$

$$\Phi_{a2} = \frac{H_m L_m - \Phi R_s}{(2R_{a2}+R_{d2})}. \tag{6}$$

The reluctances $2R_{a2}+R_{d2}$ in the path 2 are parallel to the reluctance R_{a1} in the path 1. With no moving part in the air gap, the reluctance R_{a1} of the air gap remains constant. The reluctance R_{a2} is mainly affected by the air path L_{a2} and the projected area A_{a2}, and the reluctances R_{a1} and R_{a2} are further influenced by the moving distance X of the moving part. The magnetic energy E_{a2} stored in each air path is permeated by the field strength H_{a2} and the induction B_{a2}

$$E_{a2} = \int H_{a2} B_{a2} dV = A_{a2} \int H_{a2} \cdot B_{a2} dl_{a2}. \tag{7}$$

From (6), the relationship between the induction of B_{a2} and the field strength H_{a2} is obtained as follows:

$$B_{a2} = \mu_0 H_{a2} = \Phi_{a2}/A_{a2}. \tag{8}$$

According to the principle of energy transformation, the magnetic attracting force F_x acting on the magnetic moving part in the moving direction can be obtained by the partial differentiation of the magnetic energy

$$F_x = \frac{2B_{a2}^2 A_{a2} \sin\theta \cos\theta}{2\mu_0} \tag{9}$$

where cos θ converts the inclined force from the flux direction to the acting direction of the moving part. When the moving part enters the air gap of the magnetic loop, the magnetic flux Φ_{a1} begins to diminish, and the magnetic flux Φ_{a2} starts to augment. Since the acting angle θ increases asymptotically to 90°, the magnetic attracting force F_x then loses its strength gradually. Furthermore, to achieve an effective transformation from force into torque, the magnetic force F_x must be directed tangentially toward the circumference of the rotating disk. In this dynamic process, a partial flux flows to and fro between the air gap and the working path as the reluctances change cyclically. Based on the total magnetic flux Φ described in (4), the magnetic induction B_m of the permanent magnet is then determined by

$$B_m = \Phi/A_m = \frac{H_m L_m}{A_m\left(R_s + \frac{R_{a1}(2R_{a2}+R_{d2})}{R_{a1}+2R_{a2}+R_{d2}}\right)}. \tag{10}$$

When the moving part is far away from the air gap, the entire magnetic loop is subjected to a condition with maximum reluctance, and the induction of the magnet $B_{m,\min}$ is at its minimum

$$B_{m,\min} = \frac{H_m L_m}{A_m (R_s + R_{a1})} \tag{11}$$

where the operating point of $A(H_{m,\min}, B_{m,\min})$ is located on the linear demagnetization curve of NdFeB magnet, which can be expressed by

$$\frac{H}{-H_c} + \frac{B}{B_r} = 1. \tag{12}$$

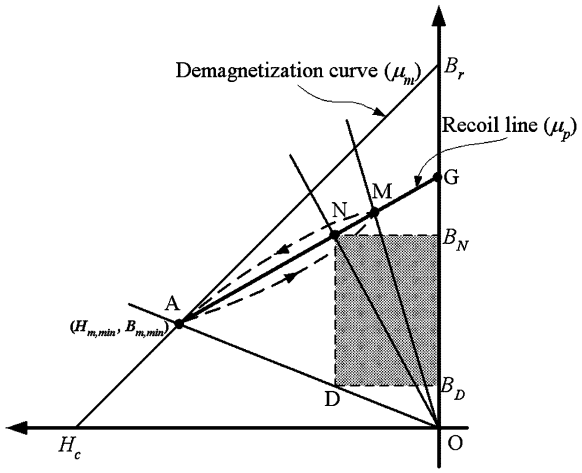

Fig. 6. Operating points and energy relationships of the permanent magnet.

Furthermore, through the relative permeability μ_m, the linear demagnetization curve between the remanent induction B_r and the coercivity H_c is described as

$$B_r = -\mu_0 \mu_m H_c. \tag{13}$$

The magnetic circuit reaches the minimum reluctance as the moving part stays inside the air gap; therefore, the induction of the magnet reaches the maximum $B_{m,\max}$ to get the operating point $M(H_{m,\max}, B_{m,\max})$

$$B_{m,\max} = \Phi / A_m = \frac{H_m L_m}{A_m (R_s + (2R_{a2} + R_{d2}))}. \tag{14}$$

From the minimum induction $B_{m,\min}$ to the maximum induction $B_{m,\max}$, the operating states of the magnet are connected to become a recoil curve, which is lower than the demagnetization curve. And the recoil curve can be deduced with the following equation:

$$(B - B_{m,\min}) = \mu_p \cdot (H - H_{m,\min}) \tag{15}$$

where the relative permeability of the recoil loop μ_p is slightly smaller than that of the demagnetization curve μ_m.

The operating points of the permanent magnet are defined along the demagnetization curve and the recoil line as shown in Fig. 6. The triangle area of OAG represents the available magnetic energy in the air gap per unit volume of the permanent magnet. In order to avoid frictional contact, a small air gap is set up between the moving part and the magnetic circuit. The gray marked triangle OAM is the total equivalent field energy of the magnet for transforming into mechanical work, which is realized by the magnetic attracting force F_x along distance X. And at the point N between the points A and M, the magnetic attracting force reaches the maximum $F_{x,\max}$, where the equivalent magnetic energy of NDB_DB_N becomes the maximum. Besides, the angular term of $(\sin\theta \times \cos\theta)$ in (9) obviously is associated with the emerging position of the maximum magnetic force.

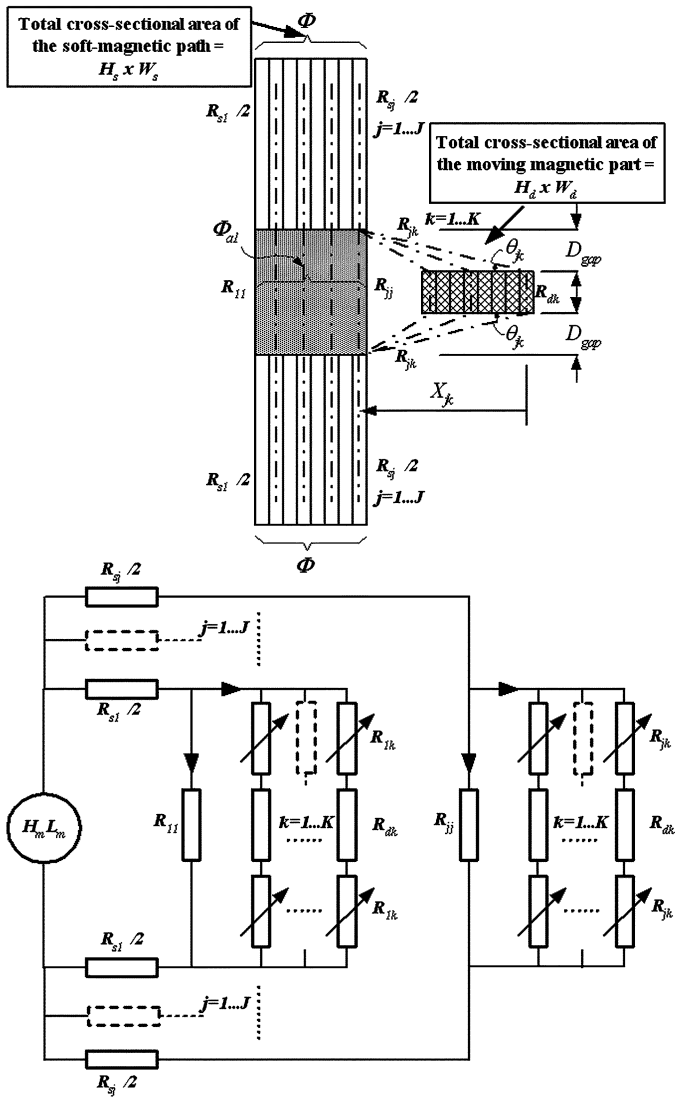

Fig. 7. Modified analytical model of magnetic circuit.

According to our preliminary analysis, the simplified equation (9) results in significant deviations on peak values and their corresponding positions, compared with the experimental results. The main reasons of these deviations are: (a) negligence of leakage fluxes and (b) inhomogeneous distribution of magnetic flux over the cross section along the magnetic loop. Taking the inhomogeneous flux into consideration, we modify the analytical model through slicing of the magnetic parts along the flux direction. Fig. 7 shows the modified analytical model in the finite slicing method, the subscripts j and k are the numbers of the sliced magnetic circuits and the sliced moving parts, respectively.

Their corresponding reluctances can be rewritten as follows:

$$\begin{aligned} &\text{Soft-magnetic path: } R_{sj} = L_s/(\mu_0 \mu_s A_{sj}); \\ &\quad A_{sj} = H_s W_s / J \\ &\text{Moving magnetic part: } R_{\mathrm{dk}} = L_d/(\mu_0 \mu_d A_{\mathrm{dk}}); \\ &\quad A_{\mathrm{dk}} = H_d W_d / K \end{aligned} \tag{16}$$

where A_{sj} and A_{dk} are the cross-sectional areas of slicing elements with a total cross-sectional area of $H_s(\text{long}) \times W_s(\text{wide})$ for the magnetic circuit and $H_d \times W_d$ for the moving part respectively. In total there are j × k possible combinations of air paths between the magnetic circuit and the moving part, and the corresponding reluctances R_{jk} are as follows:

$$R_{jk} = L_{jk}/(\mu_0 A_{jk} \sin\theta_{jk}) \tag{17}$$

where L_{jk} denotes the air path between the jth slice of the magnetic circuit and the kth slice of the moving part, $(A_{jk} \times \sin\theta_{jk}))$ is the average projected cross-sectional area, and θ_{jk} is the angle between the magnetic flux Φ_{jk} and the force acting direction

$$\begin{aligned} \theta_{jk} &= \arctan\left(D_{\text{gap}}/X_{jk}\right) \\ \text{where } X_{jk} &= X - \frac{H_s}{2}\left(\frac{1+J-2j}{J}\right) - \frac{H_d}{2}\left(\frac{1+K-2k}{K}\right) \\ j &= 1 \ldots J; \quad k = 1 \ldots K. \end{aligned} \tag{18}$$

The magnet flux Φ is then modified as the following equation:

$$\Phi = \Phi_{a1} + \Phi_{a2} = H_m L_m/(R_{\text{total}}) \tag{19}$$

where R_{total} is the total reluctance of parallel sliced magnetic paths

$$R_{\text{total}} = \frac{1}{\sum_{j=1}^{J} \frac{1}{R_{sj} + \frac{1}{(1/R_{jj}) + 1/\text{Min}\left[\left(2R_{jk}+R_{dk}\right)_{k=1\ldots K}\right]}}}. \tag{20}$$

The flux permeates through the path having the minimum reluctance, we assign the term of $\text{Min}[(2R_{jk} + R_{dk})_{k=1\ldots K}]$ to indicate the minimum reluctance within all parallel combinations of $(2R_{jk} + R_{dk})_{k=1\ldots K}$. Accordingly, the main branched fluxes Φ_{a1} and Φ_{a2} are derived

$$\Phi_{a1} = \left[H_m L_m - \Phi \Big/ \sum_{j=1}^{J}(1/R_{sj})\right] \cdot \sum_{j=1}^{J}(1/R_{jj}) \tag{21}$$

$$\begin{aligned} \Phi_{a2} = &\left[H_m L_m - \Phi \Big/ \sum_{j=1}^{J}(1/R_{sj})\right] \\ &\cdot \sum_{j=1}^{J}\{1/\text{Min}[(2R_{jk} + R_{dk})]_{k=1\ldots K}\}. \end{aligned} \tag{22}$$

From these fluxes, we can then calculate the corresponding induction B_{jk} of each air path

$$\begin{aligned} B_{jk} &= \Phi_{jk}/A_{jk} \\ &= \left[H_m L_m - \Phi \Big/ \sum_{j=1}^{J}(1/R_{sj})\right] \\ &\quad / \{A_{jk} \cdot \text{Min}[(2R_{jk} + R_{dk})_{k=1\ldots K}]\}, j = 1 \ldots J. \end{aligned} \tag{23}$$

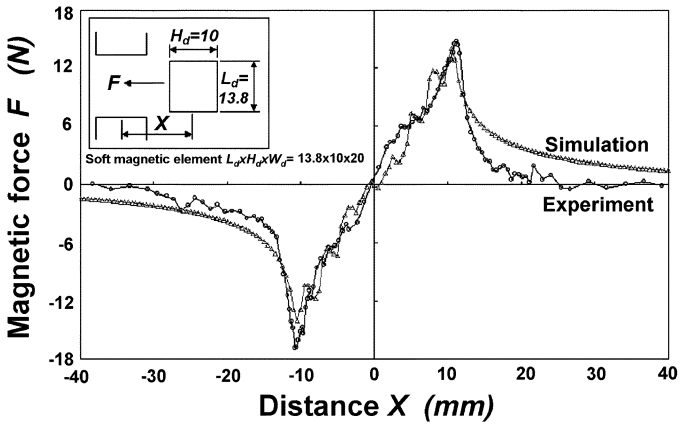

Fig. 8. Magnetic force versus moving distance. (Experiment versus analytical simulation.)

Therefore, the total magnetic attracting force acting on the magnetic moving part in the moving direction can be deduced

$$F_x = \sum_{j=1}^{J} B_{jk}^2 A_{jk} \sin\theta_{jk} \cos\theta_{jk}/\mu_0. \tag{24}$$

Fig. 8 shows the relationship between the magnetic force and the moving distance for the first type of magnetic arrangement, in which the simulation curve derived from the modified analytical model is quite consistent with the experimental curve. According to these verified equations, the relationships between design parameters and their effects on the magnetic force are summarized in Table 1. The peak's position is mainly dependent on the pole shapes of the moving part and the magnetic loop; in contrast, the curve form and the peak value are significantly related to most design parameters such as the arrangement and material of magnet, material of soft-magnetic element, magnet dimensions, pole dimensions, and air gap.

Compared with the above-mentioned theoretical analysis, the finite-element software ANSYS is an efficient tool for analyzing the kind of magnetic torque compensator with a complicated form. We choose the Solid 98(Tetrahedral Coupled-field Solid) as a basic analytical element because of its good meshing and mesh-coupling possibility. The air volume around the magnetic system is defined to prescribe an appropriate analytical zone. For optimal model meshing, the free-mesh and the smart mesh methods are applied complementarily in coordination with each other. Based on the flux analysis for each moving state, the magnetic force acting on the magnetic moving part can be derived through the virtual work. The simulation obtained through our developed finite-element model reveals a good consistency with the experimental results, as shown in Fig. 9. However, there are still some tiny deviations originated from incomprehensive consideration of the nonlinear magnetic effect, variable relative permeability, leakage flux, and distortion of meshing element in small air gap.

Besides the geometric parameters, the magnetic arrangement is also one of the main factors affecting the formation and the

TABLE I
RELATIONSHIP BETWEEN DESIGN PARAMETERS AND THEIR EFFECTS

Affected item	Curve form	Peak value	Peak's position
Arrangement and material of magnet	⊙	⊙	
Magnet dimensions	⊙	⊙	
Material of soft magnetic element	⊙	⊙	○
Pole shape	○	○	⊙
Pole dimensions	⊙	⊙	○
Air gap	⊙	⊙	○

⊙: Prior relationship ○: Secondary relationship

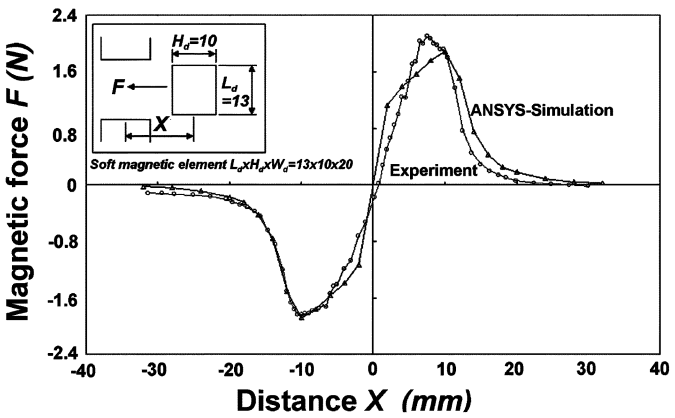

Fig. 9. Magnetic force versus moving distance. (Experiment versus FEM simulation.)

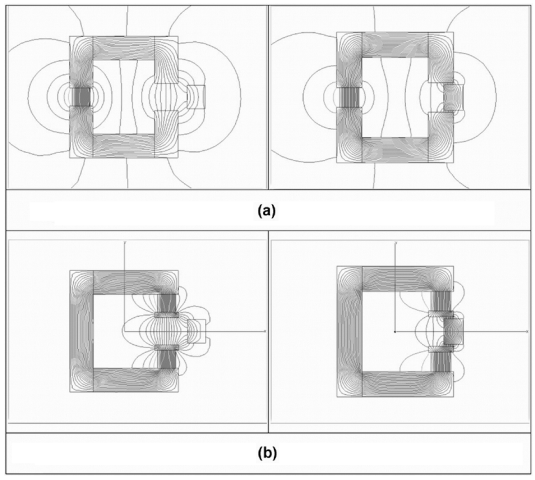

Fig. 10. Influences of magnetic arrangements. (Simulation by finite element method.) (a) Symmeatrical arrangement with one central NdFeB magnet. (b) Symmetrical arrangement with two front-installed NdFeB magnets.

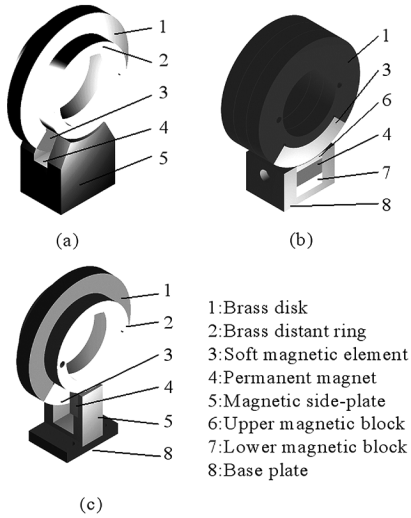

Fig. 11. Three different types of magnetic arrangements. (a) Axial type. (b) Radial type. (c) Proximate type.

variation of magnetic flux. In comparison with the central installed magnet, the front installed magnets generate more magnetic flux on the approaching soft-magnetic element as shown in Fig. 10.

C. Structure and Function of Magnetic Torque Compensator

By using modular construction, we develop a magnetic torque compensator capable of synthesizing any compensating torque compatible to all features of the roller gear cam. Main functional elements of this system are the magnetic energy source, the field guide, and the acting element. The magnetic energy source can either be a magnetic coil or a permanent magnet. Although a permanent magnet has less operational restriction than a coil due to no thermal resistance loss, a strong permanent magnet manufactured by powder metallurgy is very brittle for machining. To guide the magnetic flux of permanent magnet efficiently into a certain working zone, we apply easy-machined soft-magnetic material as field guide and acting element. The acting element is fixed on a paramagnetic disk. When the disk rotates, the acting element attracts magnetic flux out of the working zone to generate a reaction torque on the rotating disk. According to the basic concept shown in Fig. 2, we develop three different types of magnetic loops: the axial type, the radial type, and the proximate type as shown in Fig. 11. Both the axial type and the proximate type present a U-shaped working zone, and the motion directions of their acting elements are perpendicular to the flux directions of their magnetic loops. In the radial type, the working zone is set up around the circumferential surface on the rotating disk, and most magnetic flux flows from the concave surface of the magnetic loop to the circumferential surface of the magnetic rotating element.

The main groups of the rotational magnetic torque compensator are: 1) the magnetic loop equipped with permanent magnets and soft-magnetic side-plates; 2) the magnetic acting group on the shaft; and 3) the housing. To synthesize the compensating torque curve, we apply the modular system concept for easy modification of the magnetic loop and the magnetic acting group. The rotating shaft with the magnetic acting group is located within the center of the system; and the magnetic loop is installed radially around the shaft. For supporting and protecting

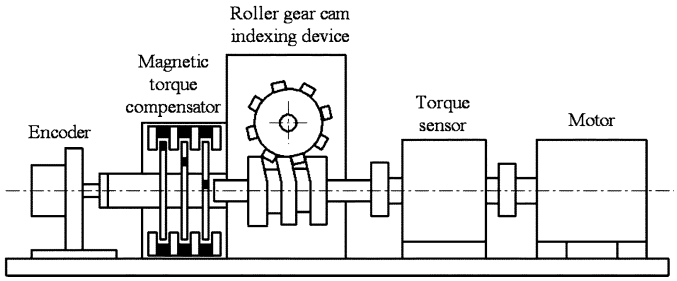

Fig. 12. Experimental installation of the magnetic torque compensator.

the entire system, a separable housing is used to fix and cover the magnetic loop and to acquire easy tuning possibility for the magnetic system.

III. Experimental Research

Fig. 12 shows the experimental installation of the magnetic torque compensator. The shaft of magnetic torque compensator is directly coupled with the input shaft of the indexing device, and the housing of the magnetic loop is fastened on that of the indexing device. The encoder for measuring rotating angle is attached to the extension rod of the magnetic torque compensator, and the torque sensor is coupled on the other side of the input shaft. The indexing device, the torque sensor, and the encoder are installed in series on the same base plate to accomplish a stable experimental condition. For acquiring the relationship between the magnetic torque and the rotating angle, the torque signal and the angular signal are simultaneously transmitted to a computer through corresponding signal conditioners and digital acquisition interface.

1) Serial Arrangement: The serial arrangement as shown in Fig. 11(a) is a modification of the axial type of magnetic arrangement; Fig. 13 shows the magnetic torque curve of the first working zone in the serial arrangement of magnets with identical magnetic orientations. The magnetic torque shows a sinus-formed curve. As the acting element enters or leaves the working zone, the maximum magnetic torque T_i or T_o exerts on the acting element, respectively. At the entrance or the exit edge of the working zone, most magnetic flux flows to the acting element, which consequently makes the tangential magnetic force reach its maximum. Under the hysteresis effect of magnetic materials, the leaving torque T_o is about 1.5 times the entering torque T_i. As the acting element completely gets into the working zone, the magnetic force acts perpendicularly to the rotating direction of the shaft and engenders no reaction torque. The little ripples on the curve come from angular vibrations induced by ball bearings. Because of the opposite polarization on both sides of the magnetic side-plate, the flux is chiefly built up inside the magnetic side-plates except the working zone. The flux density at the margins is lower than that in the midst of the working zone. This inhomogeneous distribution of flux density and the magnetic interaction between adjacent working zones bring torque augmentation unproportionate to the increase of working zones.

Fig. 14 shows the magnetic torque curve of the first working zone in the serial arrangement of magnets with opposite magnetic orientations. Inside each magnetic side-plate, the magnetic

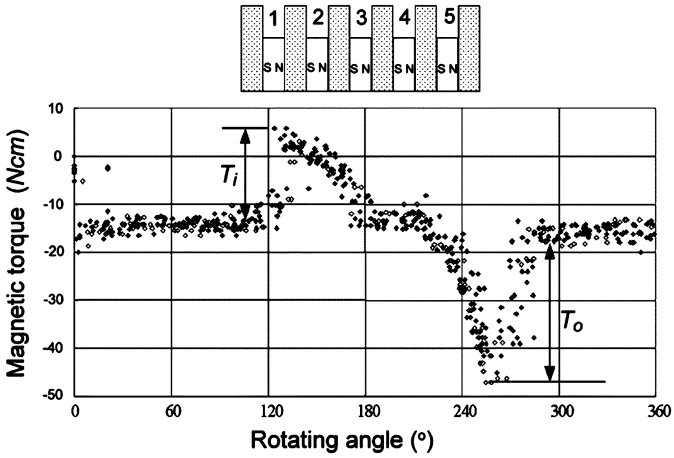

Fig. 13. Magnetic torque curve from the first working zone in the serial arrangement of magnets with identical magnetic orientations.

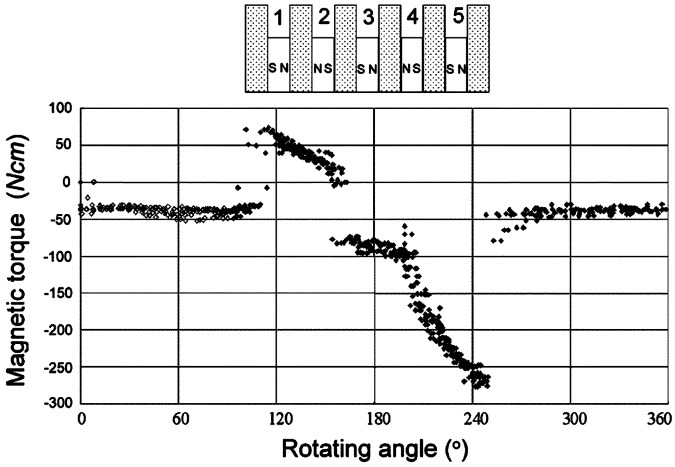

Fig. 14. Magnetic torque curve from the first working zone in the serial arrangement of magnets with opposite magnetic orientations.

repulsion drives most of the magnetic flux to the working zone through the designed magnetic loop. The flux density in the working zone is four times that of the above-mentioned magnetic arrangement with the identical orientations. And the magnetic force increases in proportion to the energy transformation between the magnetic and the mechanical energy. Furthermore, the magnetic hysteresis effect enlarges the leaving torque T_o to about two times the entering torque T_i. The opposite orientations of magnets keep a constant flux density in each working zone, and such arrangements also prevent interference from adjacent working zones. Accordingly, the magnetic torque can be summed up in proportion to the increase of the working zones.

Through suitable arrangement of the acting elements and the rotating disks, diverse torque curves can be synthesized on the basis of the curve unit. Fig. 15 presents the simulated induction distributions on the 3-D models for two sequential states with finite-element method. In contrast to the magnets with identical orientations, these with opposite orientations allow more magnetic energy to flow to the edges of the magnetic side-plates and the air gap.

2) Radial Arrangement: The other alternative design concept is the radial arrangement shown in Fig. 11(b), where the

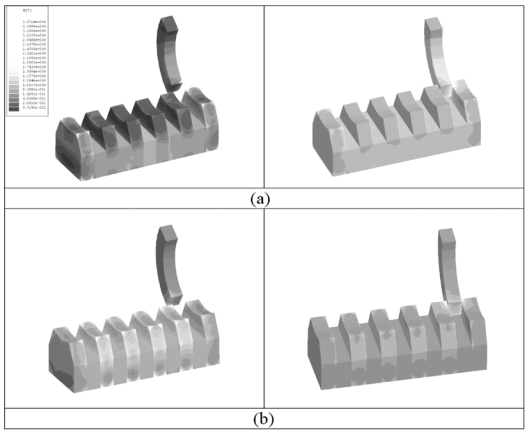

Fig. 15. Influences of magnetic orientations in serial arrangement of magnets. (Simulation by finite element method). (a) Serial arrangement of magnetes with identical magnetic orientations. (b) Serial arrangement of magnetes with opposite magnetic orientations.

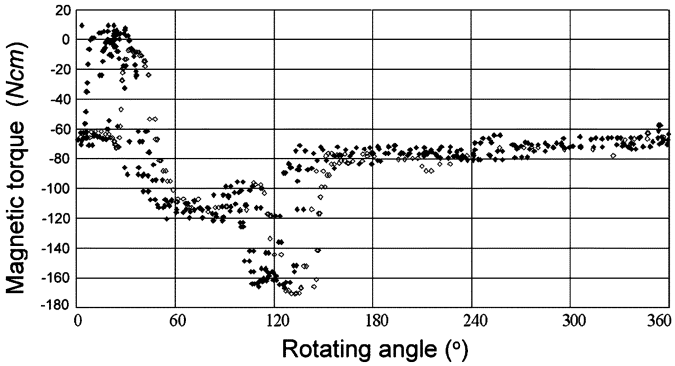

Fig. 16. Magnetic torque curve of radial arrangement with 0.3 mm air gap.

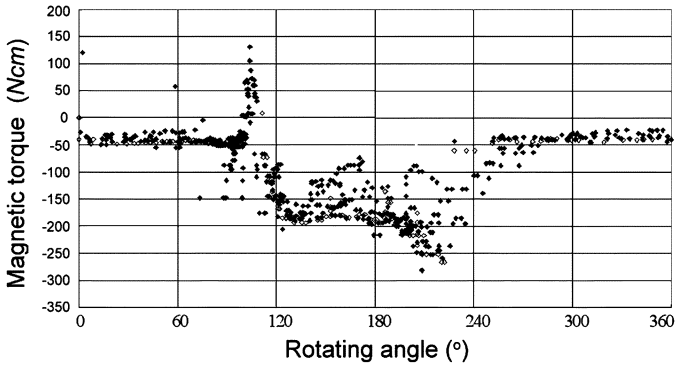

Fig. 17. Magnetic torque curve of proximate arrangement.

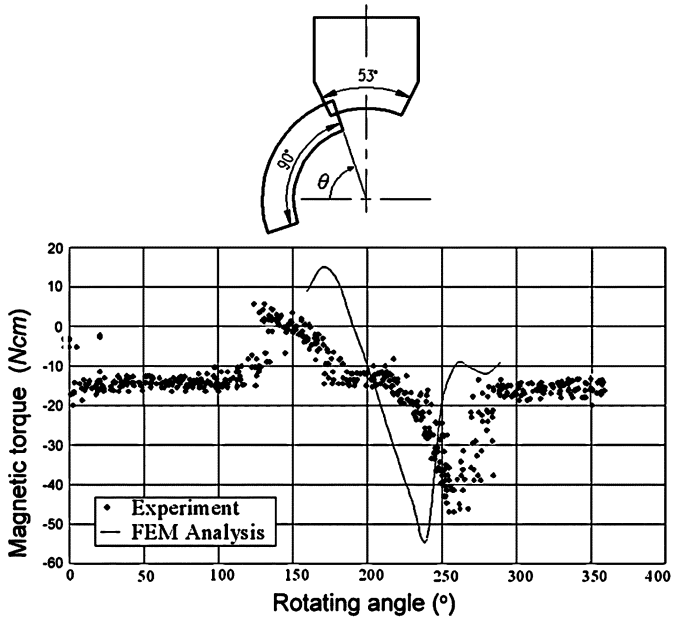

Fig. 18. Magnetic torque curve of a serial arrangement. (Experiment versus FEM simulation.)

soft-magnetic block leads the flux of the permanent magnet to the circumferential surface on the rotating disk. For achieving field guiding tangentially toward the rotating direction, the soft-magnetic block is machined to match the circumference of the rotating disk. As shown in Fig. 16, the relationship between the magnetic torque and the rotating angle is quite different from those of the serial arragements. When the acting element enters into or comes out of the working zone, the magnetic torque curve changes drastically and marks higher amplitude than that in the serial arrangement due to the short reaction time. Because of backlash and mounting errors, the unintended inclination of the radial gap between the stator and the rotor gives rise to the asymmetry of the magnetic torque curve.

3) Proximate Arrangement: Based on our previous theoretical and experimental analyses, we verified that a magnet allows more flux directly to permeate the working zone without any intermediate soft-magnetic medium. Fig. 11(c) presents our proximate arrangement, where two permanent magnets are fixed face to face to build up a U-shaped working zone for the rotating disk. Fig. 17 shows the measured torque curve. In spite of high field strength in the working zone, the magnetic torque is unexpectedly small here, because most flux of NdFeB magnet comes directly out of its pole surfaces, and much less magnetic flux permeates from its circumferential surfaces to the approaching acting element. In addition, mounting inaccuracies and magnetic hysteresis can induce the asymmetry of the curve.

Fig. 18 shows the experimental results versus the simulation results of the serial arrangement derived through finite-element method; there are significant differences on the peak values and the corresponding positions. The experimental and simulation curve have almost the same energy area under the torque curves, but the angular range of the simulation curve is narrower than that of the experimental curve because the magnetic flux distributes over a larger space than that predicted by the simulation.

In order to comprehend the curve-synthesizing performance, simulations are made to study the influence of the working area of the acting element on the torque. The working area of the magnetic loop covers an angular sector of 53°, and each acting element has an angular sector of 3° in rotating direction. Being regarded as a basic element, the acting element can be linked together to form a large element or be arranged radially on the rotating disk. The simulation results presented in Fig. 19 reveal that the magnetic torque changes in proportion to the working area variation. Therefore, any torque curve can be synthesized

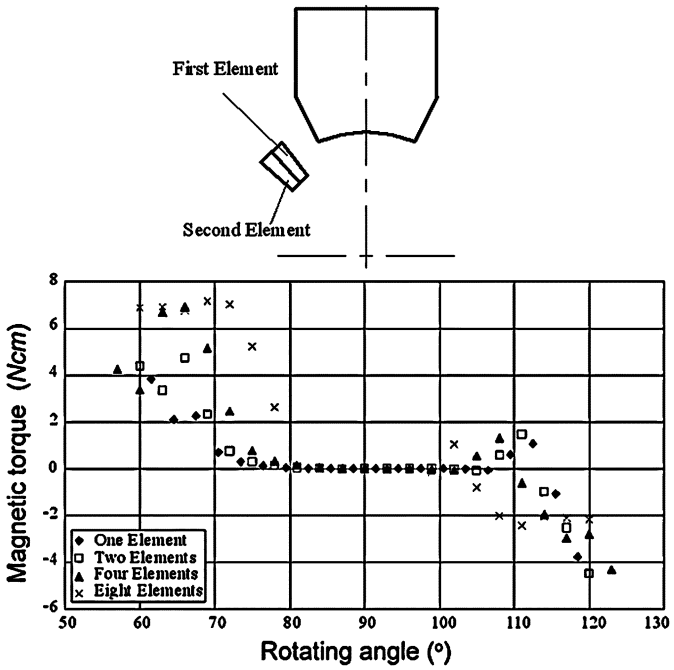

Fig. 19. Influence of magnetic working area on the torque curve.

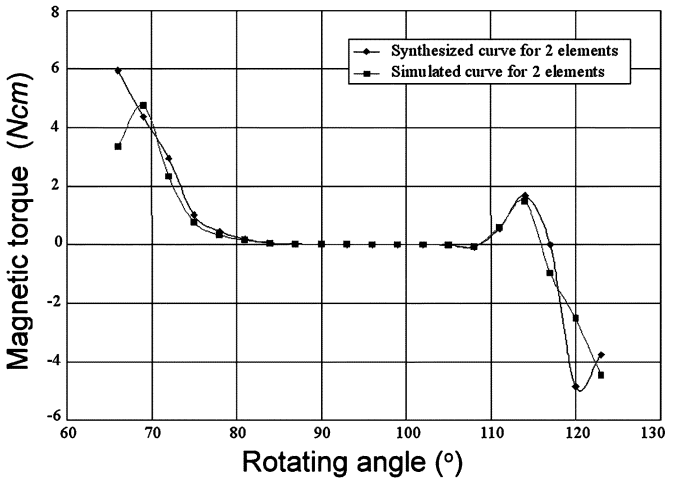

Fig. 20. Simulated curve versus synthesized curve of two linked acting elements.

directly through suitable arrangement of elements as mosaics on the rotating disk.

As Fig. 20 shows, except small deviations of the two linked acting elements, there is no obvious difference between the simulated curve and the synthesized curve.

Either through experiment or finite-element analysis (FEA), we can acquire a magnetic torque curve of each acting element. And by analogy with mosaic buildup, we can arrange acting elements to construct any desired torque curve. To obtain a larger torque, we can put an acting element in a large radial position, or install several acting elements on parallel rotating disks, respectively. To extend the span of the both peaks, we can either set acting elements in series along the circumference of a rotating disk or in successive order on some parallel disks. Fig. 21

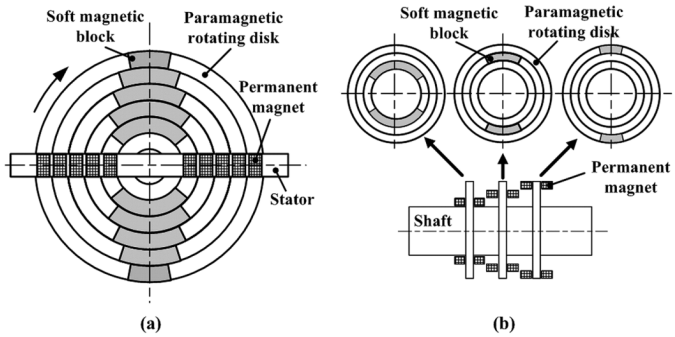

Fig. 21. Two design schemes of magnetic torque compensators. (a) Concentrical arrangement. (b) Axially parallel arrangement.

illustrates two different design schemes: one with concentrical arrangement, and the other with axially parallel arrangement. Certainly, it is also possible to integrate those advantages of both arrangements to create a hybrid type.

IV. Conclusion

To compensate the torque variation on the input shaft of indexing devices, we adopted the magnetic working principle to develop magnetic torque compensating devices. The magnetic energy from the permanent magnet is transformed into the mechanical torque on the rotating magnetic element. Different types of magnetic loops and their characteristics are comprehended through experiments and analyses with the equivalent magnetic circuit and the finite-element method. A serial arrangement with identical magnetic orientations, in spite of its installing convenience, generates less magnetic flux for energy transformation. The modified serial arrangement with opposite magnetic orientations allows magnetic flux to permeate effectively into the working zone, and it also realizes higher magnetic torque. Having more efficient energy transformation, the radial arrangement demands more efforts to arrange the curvy working zone and the rotating disk. In the proximate arrangement, the permanent magnets, placed in the proximity of both sides of the rotating disk, transmit the magnetic energy directly to the acting element; while the flux of NdFeB magnet, coming mainly from the pole surface, creates less magnetic torque in tangential direction. The modular configuration of the magnetic torque compensator enables different types of the magnetic loops to be integrated to adapt to diverse technical requirements. By means of curve synthesis, any compensating torque curve demanded can be built up by appropriate arrangement of magnets or magnetic acting elements in the torque compensator.

Acknowledgment

This work was supported by the National Science Council of Taiwan under Grant NSC 88-2622-E-110-001. The authors would like to thank Tan Tzu Precision Machinery Co., Ltd. for their financial and technical support.

References

[1] S. K. Georgieff, "Follower Positioning and Indexing Cam for Roller Gear Drive and Method of Use," U.S. Patent 3 817 16, Jun. 18, 1974.

[2] D. M. Tsay and B. J. Lin, "Design and machining of globoidal index cams," *ASME J. Manuf. Sci. Eng.*, vol. 119, pp. 21–29, 1997.
[3] E. J. Sarring, "Torque compensation for cam systems," in *Trans. 7th Conf. Mechanisms*, Oct. 8–10, 1962, pp. 179–185.
[4] C. E. Benedict, G. K. Matthew, and D. Tesar, "Torque balancing of machines by sub-unit cam systems," in *Second Appl. Mechanisms Conf.*, Oklahoma State University, Stillwater, Oct. 1971, pp. 15-1–15-3.
[5] M. Nishioka and M. Uchino, "Compensation of input shaft torque on indexing cam mechanisms," *Trans. Jpn. Soc. Mech. Eng., Ser. C*, vol. 59, no. 562, pp. 1913–1919, 1993.
[6] M. Nishioka, "Compensation of input shaft torque on indexing cam mechanisms (2nd report, verification of the theory)," *Trans. Jpn. Soc. Mech. Eng., Ser. C*, vol. 60, no. 569, pp. 338–342, 1994.
[7] M. Nishioka and M. Yoshizawa, "Compensation of input shaft torque on indexing cam mechanisms (3rd report, correction by inertia term for compensating system with deminaut spring force)," *Trans. Jpn. Soc. Mech. Eng., Ser. C*, vol. 60, no. 576, pp. 2830–2836, 1994.
[8] D. M. Tsay, H. C. Ho, and K. C. Wang, "Design of torque balancing cams for globoidal cam indexing mechanisms," *ASME J. Mech. Des.*, vol. 124, pp. 441–447, 2002.
[9] Y. S. Kwon, H. Y. Hwang, H. R. Lee, and S. H. Kim, "Rate loop control based on torque compensation in anti-backlash geared servo system," in *Proc. Amer. Control Conf.*, Boston, MA, Jun. 30–Jul. 2, 2004, pp. 3327–3332.
[10] M. Odai and Y. Hori, "Speed control of 2-interia system with gear backlash using gear torque compensator," in *Proc. IEEE Int. Workshop on Advanced Motion Control*, 1998, pp. 234–239.
[11] Y. Nakayama, K. Fujikawa, and H. Hobayashi, "A torque control method of three-inertia torsional system with backlash," in *Proc. IEEE Int. Workshop on Advanced Motion Control*, 2000, pp. 193–198.
[12] H. S. Choi, J. H. Lee, and I. H. Park, "Separation of each torque component on parts of electric machine using magnetic force density," *IEEE Trans. Magn.*, vol. 41, no. 5, pp. 1464–1467, May 2005.
[13] S.-I. Kim, J-Y. Lee, Y.-K. Kim, J.-P. Hong, Y. Hur, and Y.-H. Jung, "Optimization for reduction of torque ripple in interior permanent magnet motor by using the Taguchi method," *IEEE Trans. Magn.*, vol. 41, no. 5, pp. 1796–1799, May 2005.
[14] T.-S. Hwang, J.-K. Seok, and D. H. Kim, "Active damping control of linear hybrid stepping motor for cogging force compensation," *IEEE Trans. Magn.*, vol. 42, no. 2, pp. 329–334, Feb. 2006.
[15] L. Hadjout, N. Takorabet, R. Ibtiouen, and S. Mezani, "Optimization of instantaneous torque shape of PM motors using artificial neural networks based on FE results," *IEEE Trans. Magn.*, vol. 42, no. 4, pp. 1283–1286, Apr. 2006.
[16] J. M. Park, S. I. Kim, J. P. Hong, and J. H. Lee, "Rotor design on torque ripple reduction for a synchronous reluctance motor with concentrated winding using response surface methodology," *IEEE Trans. Magn.*, vol. 42, no. 10, pp. 3479–3481, Oct. 2006.
[17] Z. Q. Zhu, Y. Liu, and D. Howe, "Minimizing the influence of cogging torque on vibration of PM brushless machines by direct torque control," *IEEE Trans. Magn.*, vol. 42, no. 10, pp. 3512–3514, Oct. 2006.
[18] T. Ueno, C. S. Keat, and T. Higuchi, "Linear step motor based on magnetic force control using composite of magnetostrictive and piezoelectric materials," *IEEE Trans. Magn.*, vol. 43, no. 1, pp. 11–14, Jan. 2007.

Manuscript received May 30, 2005; revised April 6, 2006. Corresponding author: K.-Y. Huang (e-mail: kyhuang@ntu.edu.tw).

Kuang-Yuh Huang (M'05) received the Dipl.-Ing. and Dr.-Ing. degrees in the field of precision engineering from the Institute of Precision Engineering at Technical University Berlin, Berlin, Germany, in 1988 and 1994, respectively.

He has been an Associate Professor in the Department of Mechanical Engineering at National Taiwan University, Taipei, Taiwan, R.O.C., since 1994. His teaching and research interests include precision engineering, design of actuators and sensors, and biomedical engineering.

Dr. Huang has been a member of the Verein Deutsche Ingenieure (VDI, The Association of German Engineers) since 1986, the Chinese Society of Mechanical Engineer (CSME, Taiwan) since 1995, and the International Society of Optical Engineering (SPIE, USA) since 1999.

Pei-Chuan Lin received the M.S. degree from the Department of Mechanical Engineering at National Taiwan University, Taipei, Taiwan, R.O.C., in 1998. In 2005, he received another M.S. degree from the Department of Electrical Engineering and Computer Science, and then the Ph.D. degree from the Department of Mechanical Engineering at the University of Michigan.

Since then, he has been working as a Postdoctoral Research Fellow in the Department of Materials Science and Engineering at the University of Pennsylvania.

Sheng-Fu Tsai received the M.S. degree from the Department of Mechanical Engineering at National Taiwan University, Taipei, Taiwan, R.O.C., in 1999.

He worked as a Research Engineer at the Industrial Technology Research Institute. He now works for Foxsemicon Integrated Technology Inc., Taiwan.